



Impact statement

Although graphene is compatible with many current technologies taking advantage of its physical properties, its lack of a bandgap limits its current applications for mainstream electronics. Transition-metal dichalcogenides (TMDs) have been studied well in the past decade, with a tremendous amount funding from federal agencies and the industry, and have demonstrated multiple avenues to modulate their electronic properties, including bandgap and conductivity. Advances in arowth of two-dimensional materials enable us to deposit layered materials that are only one or few unit cells in thickness, and enabled us to fabricate novel devices. However, to realize their mainstream applications in electronics, a scalable method to develop high-quality wide-area films is necessary. Research on solution-based TMD growth has investigated the effects of different solvent systems, including additives such as polymers as dispersants and adhere the precursors to the substrate. However, these methods tend to produce rather inhomogeneous films. In this article, we propose a solution-based chelant-enhanced WS₂ TMD growth method that takes advantage of the metal precursor's complexation normally parasitic to film growth, resulting in higher-quality few-layer films. Our method offers the next step in wafer-scale TMD films that is necessary for incorporating them into semiconductor industry compatible processing.

Chelant-enhanced solution for wafer-scale synthesis of few-layer WS₂ films

Miguel Isarraraz, Pedro Pena, Mohammed Sayyad, Shize Yang, Han Li, Amir-Ali Akhavi, Mina Rashetnia, Ruoxu Shang, William Coley, Yongtao Cui, Mustafa Kurban, Sefaattin Tongay,*

Mihrimah Ozkan,*

and Cengiz S. Ozkan*

Large area growth of few-layer transitional-metal dichalcogenide thin films using a solution-based process are being considered as potentially scalable thin-film processing for future nanoelectronics. A wafer-scale growth of two-dimensional tungsten disulfide (WS₂) films with consistent uniformity still remains a challenge in all types of growth methods. Specifically, the synthesis of WS₂ using a solution-based approach has been a difficult task due to the complex surface chemistry involved. In the current study, we report on the wafer-scale synthesis of uniform WS₂ using a spin-coat process. Previously, a solvent of ethylenediaminetetr aacetic acid in DMSO with ammonium tetrathiomolybdate ((NH₄)₂MoS₄), and a thermolysis step were used to achieve uniform wafer-scale growth of few-layer MoS₂ films. Here, we present a study of three different chelating agents using dimethyl sulfoxide (DMSO) as a solvent to demonstrate the chelant's critical role in growing uniform dichalcogenide films. Of these three chelating agents, glycine consistently produced wafer-scale growth.

Introduction

Atomically thin transition-metal dichalcogenide (TMD) thin films are a class of twodimensional (2D) materials that have high interest due to their optical and electronic properties. Unlike graphene, the TMDs involving Mo-, W-, and Re-based metal cations have a direct bandgap in the 2D monolayer form that is comparable to a

Miguel Isarraraz, Department of Electrical and Computer Engineering, University of California, Riverside, USA

Pedro Pena, Department of Chemistry, University of California, Riverside, USA

Mohammed Sayyad, Materials Science and Engineering, School for Engineering of Matter, Transport, and Energy, Arizona State University, Tempe, USA

Shize Yang, Materials Science and Engineering, School for Engineering of Matter, Transport, and Energy, Arizona State University, Tempe, USA

Han Li, Materials Science and Engineering, School for Engineering of Matter, Transport, and Energy, Arizona State University, Tempe, IISA

Amir-Ali Akhavi, Materials Science and Engineering Program, University of California, Riverside, USA

Mina Rashetnia, Department of Physics, University of California, Riverside, USA

Ruoxu Shang, Materials Science and Engineering Program, University of California, Riverside, USA

William Coley, Materials Science and Engineering Program, University of California, Riverside, USA

Yongtao Cui, Department of Physics, University of California, Riverside, USA

Mustafa Kurban, Department of Electrical and Electronics Engineering, Kırşehir Ahi Evran University, Kırşehir, Turkey; Department of Prosthetics and Orthotics, Faculty of Health Science, Ankara University, Ankara, Turkey

Sefaattin Tongay, Materials Science and Engineering, School for Engineering of Matter, Transport, and Energy, Arizona State University, Tempe, USA; sefaattin.tongay@asu.edu

Mihrimah Ozkan, Department of Electrical and Computer Engineering, University of California, Riverside, USA; Department of Chemistry, University of California, Riverside, USA; mihri.ozkan@ucr.edu

Cengiz S. Ozkan, Department of Electrical and Computer Engineering, University of California, Riverside, USA; Department of Chemistry, University of California, Riverside, USA; Materials Science and Engineering Program, University of California, Riverside, USA; Department of Mechanical Engineering, University of California, Riverside, USA; cengiz.ozkan@ucr.edu cozkan@engr.ucr.edu *Corresponding author

Miguel Isarraraz and Pedro Pena have contributed equally to this work.

doi:10.1557/s43577-023-00557-w



variety of traditional semiconductors such as Si, GaAs, and SiC except they can be scaled down to the atomic level. MoS₂ and WS₂ are the most intensely studied 2D TMDs owing to their exceptional properties such as their high on/off ratios, ^{2,3} high mobility, ⁴ tunable excitonic effects, ⁵ and valleytronic physics. ^{6,7}

These TMD materials have been synthesized and prepared by laser-based thinning, 8 chemical exfoliation, 9 mechanical exfoliation, 10-12 and chemical vapor deposition. 13 Of these techniques, the most promising form of growth is through chemical vapor deposition (CVD) due to its ability to produce high-quality and large thin films. 14-17 In the growth of WS₂ by CVD, triangular structures have been observed. The growth of WS2 thin film is difficult to do due to difficulties in controlling vapor phase reaction and precursor stoichiometry from the vaporization of precursor materials. 18 The main synthesis route for WS₂ thin film is the use of ultrahigh-vacuum (UHV) deposition of a thin layer of metals or metal oxides followed by sulfurization. ¹⁹ It has been demonstrated that the challenges in uniformity of thin films can be overcome by atomic layer deposition (ALD)²⁰ but these routes require high costs. Moreover, the nucleation density remains rather high due to low processing temperatures and these films usually possess nanometer-scale single domain sizes.

A cost-effective and controllable alternative to this route is a solution-based synthesis. Thin films can be produced via a two-step thermolysis approach. The process involves coating a $(NH_4)_2MoS_4$ precursor solution onto a substrate, then decomposing it at a high temperature to produce the MoS_2 film. Several groups have developed approaches such as dip coating, ²¹ spin coating, ^{22–25} micromolding in capillaries (MIMICs), ²⁶ and polymer-assisted deposition. ²⁷ The spin-coating method has been shown as an efficient way to produce controlled layers based on the solution concentration and spin-coating parameters.

The main challenges that must be addressed in these methods are the reduction of the de-wetting area, the density of surface defects, and optimization of thin-film uniformity. Many researchers have developed different solutions based on solvents such as *N*-methyl pyrrolidone (NMP), dimethylformamide (DMF), dimethyl sulfoxide (DMSO), and others to address these issues. These methods are solely optimized for the thermolysis of (NH₄)₂MoS₄. ^{28–30} The growth of WS₂ films via thermolysis has been demonstrated for several applications. Li et al. produced thick uniform WS₂. ²⁸ Abbas et al. ³⁰ produced a large-area WS₂ by a solvent mixture of NMP, *n*-butylamine, 2-aminoethanol. Although there are many methods for thermolysis for (NH₄)₂MoS₄, thin, uniform wafer-scale WS₂ films remain a challenge.

Here, we show a chelant-enhanced solution-based synthesis of wafer-scale WS₂ thin films. In our previous study by Ionescu et al., ²⁵ a chelating agent, ethylenediaminetetraacetic acid (EDTA), was used to exert control over wafer coverage and thickness of MoS₂. In this study, three different chelating

agents were used: EDTA, glutamic acid, and glycine to produce these films. By optimizing the wettability of the solution (hydrophilicity), this study focuses on the relationship between the solution and the substrate and their effect on film coverage. This study reveals that the chelant plays an important role in the control of thickness and formation of films. Optical microscopy, SEM, and AFM were used to evaluate the uniformity and coverage of the films whereas Raman spectroscopy and photoluminescence were used to evaluate the quality. Atomic force microscopy (AFM) was used to measure the thickness of the film.

In this work, wafer-scale thin films were synthesized by the thermolysis of $(NH_4)_2WS_4$ (ATTT). The growth structures for each chelant are investigated. Three solutions were prepared in DMSO with each chelant. The concentration of the precursor was set to 45 mM with a chelant ratio of 1:2 as an excess amount of chelant will drive reaction forward. The solution was filtered to remove excess chelant. Details of the preparation of substrate and solution are described in the experimental section.

Previously, it has been shown that the chelant favorably binds to the hydroxylated surface of SiO₂ substrates. This gives the solution better wettability and provides a uniform spin coat. In solution, the chelant preferably complexes to metal centers and improves substrate wettability and film formation after 24 h. When the solution is spin coated onto the substrate, Ionescu et al. proposed the chelant anchors MoS₄²⁻ onto the surface via hydrogen bonding.²⁵ Herein, we demonstrate that the chelating agent is vital for uniform WS2 coverage: it stabilizes the WS₄²⁻ anion in solution, favorably binds to the bare SiO₂ surface improving solution wettability and evenly anchors the complex to the surface. In this system, the chelant and the metal salt solution in DMSO form a network that affects the uniformity of the thin film. The chelants differences in size and functional groups play a major role in film uniformity.

Results and discussion

UV vis data of the chelant/ATTT precursor solutions were collected to better understand the solution stability and chelation. Figure 1a shows the absorption spectra of the glycine precursor solution when it is made (yellow line) and after 24 h (blue line). The color of the solution is attributed to the $(WS_A)^{2-}$ portion of the salt. The UV-VIS spectra of the solution of the ATTT chelated complex at 0 h revealed two absorption peaks at 275 nm, and 395 nm. The two absorption bands at 275 nm and 395 nm can be associated with those of the tetrathiotungstate ions $(WS_4)^{2-}$, whereas an absorption band at 335 nm can be attributed to WOS₃^{2-.31} It was shown the chelating agents (such as EDTA) can favorably bind to molybdenum and its sulfides, help disperse them, and prevent their oxidation.³² Tungsten as a group six element (much like molybdenum) reacts in similar matter as evident by the lack of growth in the oxide peak at 335 nm suggesting WS₄²⁻ passivation. Without the chelating agent, the expected reaction between O²⁻ ions

in the solution and WS_4^{2-} could be validated in the small peak at 335 nm. The formation of more oxidized forms would lead to tungstate polymerization, which directly competes with chelation.³³ This oxidization has been shown in other similar reactions.^{31,34}

The chelant/ATTT mixture in DMSO is a yellow solution that can be spun coat, but produces incomplete films as it hasn't had time to fully chelate yet. After 24 h, there is a marketed change in color and the UV-vis spectra shows an additional peak at 635 nm. If we look at absorption bands of liquid exfoliated WS₂, there are two absorption bands associated with the material.³⁵ The absorptions at 535 nm and 646 nm are the bands associated to WS₂. Although the broad peak at 635 nm could overlap with 646 nm, it is a poor match because it lacks the absorption band at 535 nm indicating there is no WS₂ present in solution. It is difficult to associate this band with other materials such as WS₃ due to this material being an intermediate product during heating. After 24 h, the color changes from a bright yellow solution to a yellow brown. The change of color could be an indication that the (WS₄)²⁻ cluster is chelating as it does not change in the absence of a chelating agent.

After 24 h, and having had sufficient time to react, the glycine solution readily wets the substrate and produces uniform films. To get a better understanding of these processes, two different glycine solutions were prepared. The first glycine precursor solution contains DMSO as a solvent while the other contains water. The samples are prepared using the same procedures, placed in storage, and inspected after 24 h. When inspected, the DMSO solution showed a change in color while the water solution showed no change in color. The DMSO solution becomes more acidic (pH changes from 7 to 6) while the

water solution stays the same pH. For the DMSO solution, this is likely the result of the deprotonation of the carboxylic acid into a carboxylate chelating active site. Glycine forms a zwitterion in water, forming the carboxylate group, which assists in wettability but occupying the amino group lone pair with a proton that hinders chelation. ³⁶ Films were synthesized for each solution shown in Figure 1b-c. As we can see in Figure 1b, the water solvent precursor films consisted of large, dense clusters of structures throughout the substrate. From Figure 1c, we see that the DMSO solution produced film at a large scale. In these two solutions, the solvent plays a strong role in the formation of the chelated compound and by extension the resulting film quality. The lack of complete color change also suggests chelation between ATTT and glycine does not readily occur in water. In this case, the ATTT has no molecule to evenly anchor it to the SiO₂ substrate, thus not preventing the aggregation that causes clustered islands to form. In the DMSO solution, there was an increase of chelant binding to $(WS_4)^{2-}$ clusters thus allowing the ATTT complex to anchor to the surface more evenly. Interactions between the chelants and SiO2 were probed via DFT to confirm favorable chelant and bare SiO₂ coordination.

First, DFT calculations were performed to better understand the interactions between the $SiO_2/Si(100)$ substrate and chelating agents (EDTA, glutamic acid, and glycine). Because the majority of this surface is unhydroxylated, with there being approximately five OH groups per square nanometer in a fully hydroxylated surface, ³⁷ we probed an unhydroxylated surface to see if binding was still favorable without the OH groups. In this context, the binding energies (E_b) were calculated based on the structure with the lowest total energy. The E_b values were found to be 2.85, 2.42, and 0.89 eV for SiO_2 —EDTA,

SiO₂-glutamic acid, and SiO2-glycine systems, respectively. This result shows that E_h increases with the size of chelating agents due to the increased number of bonds, which means the number of interacting atoms increases with size. This also represents that the EDTA tends to bind with the SiO₂ surface more effectively compared to glycine and glutamic acid. In Figure 2, we see that for the three cases oxygen atoms in chelating agents tend to interact with Si atoms on the SiO₂ surface 80 μr with the distances 1.88, 1.68, and 1.98 Å and angle between the two O atoms in the chelating agents are 124°, 121°, and 123° for EDTA, glutamic acid,

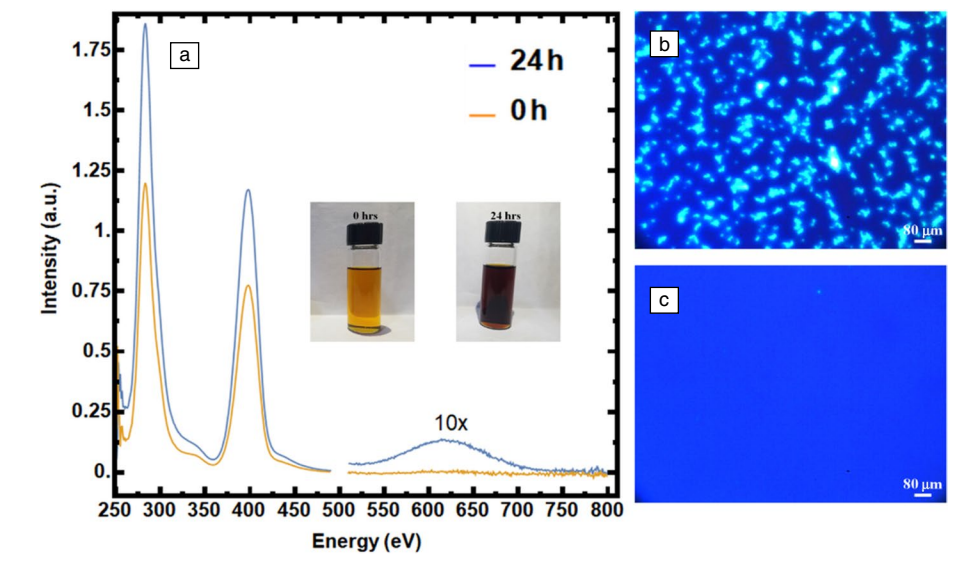


Figure 1. (a) UV–vis of glycine in DMSO with precursor solution. At t=0 h, the solution is golden yellow. Two absorption peaks are present at 280 eV and 380 eV. At t=24 h, the solution has darkened, and a new absorption peak is observed at 625 eV. (b) Optical image of WS $_2$ using water as a solvent. (c) Optical image of WS $_2$ using DMSO as a solvent.

and glycine, respectively. In the

last part of DFT calculations,



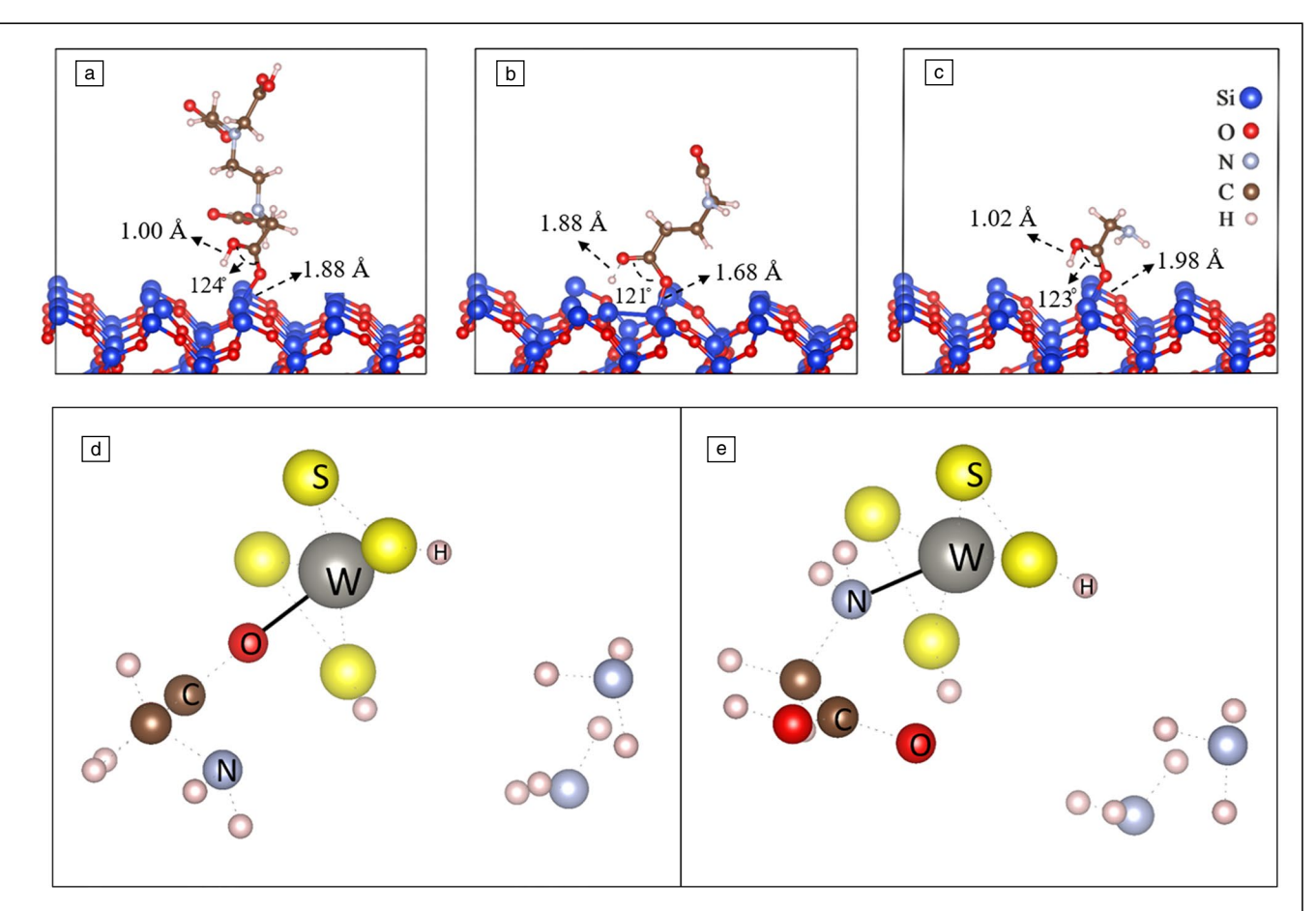


Figure 2. Interactions between the $SiO_2/Si(100)$ surface and chelating agents: (a) EDTA, (b) glutamic acid, and (c) glycine. (d, e) The interactions between ammonium tetrathiotungstate [(NH₄)₂WS₄] and glycine in DMSO; (d) shows initial bonding/coordination via the oxygen on glycine; (e) shows bonding/coordination initiated by the nitrogen atom.

the interactions between the three chelants glycine, glutamic acid, and EDTA and metal ions of (NH₄)₂WS₄ in DMSO were performed. As an example, the interactions between glycine and (NH₄)₂WS₄ are given in Figure 2d–e. Here, the oxygen (D) and nitrogen (E) atoms on the two ends of the chelant have been interacted with the metal ions in the center of (NH₄)₂WS₄ in DMSO. The predicted binding energy (E_b) values were found to be 1.132, 3.022, and 1.399 eV for binding to the O atoms of the chelating agents glycine, glutamic acid, and EDTA to the metal ion, respectively. When it comes to binding N atoms of glycine and glutamic acid, the E_b were found to be 3.055 and 3.543 eV, respectively. For EDTA, only one case was considered because its two ends include O atoms. These results suggest that N atoms in the chelants tend to bind the metal ions of $(NH_4)_2WS_4$ more effectively than that of O atoms. Also, the glutamic acid and the metal ions of (NH4)₂WS₄ have higher E_h value than glycine. From the calculations, we see that EDTA should bind more effectively to SiO₂ than glutamic acid or glycine, whereas glutamic acid binds more strongly to the WS₄²⁻ ions. Our findings show that EDTA produced no film (only large structures), and glutamic acid produced an uncomplete film, whereas glycine produced a full film. In all cases, the

solutions readily and evenly wet the SiO_2 substrate, but not all chelating agents readily anchor the WS_4^{2-} precursor.

The uneven (glutamic acid) and incomplete anchoring (EDTA) suggest there are other factors that inhibit chelation. This is likely due to the relative size of the three chelating agents, as their size could exclude access to nearby anchoring sites on the SiO₂ surface. The active sites for these chelating agents are the carboxylic acid/carboxylate (when deprotonated) groups and the neighboring amino group.³³ EDTA also has multiple active sites, which could lead to over-complexing and thus poor to no film coverage. From the calculations, we also see that the E_h of O on glutamic acid to metal center is comparable to the E_b of the N on glycine to metal center. We can expect glutamic acid to therefore have some factor of over-complexing and occupy the oxygen sites that help evenly anchor the complex to the surface. Another consideration is the reaction conditions for the ATTT chelation. EDTA and glutamic acid are both weak acids and produce more acidic protons than glycine. Chelation is sensitive to pH as protons can inhibit metal center-ligand coordination. This is especially so for tungsten complexing as there exists a parasitic tungstate self-polymerization reaction.³³ Film coverage and quality of

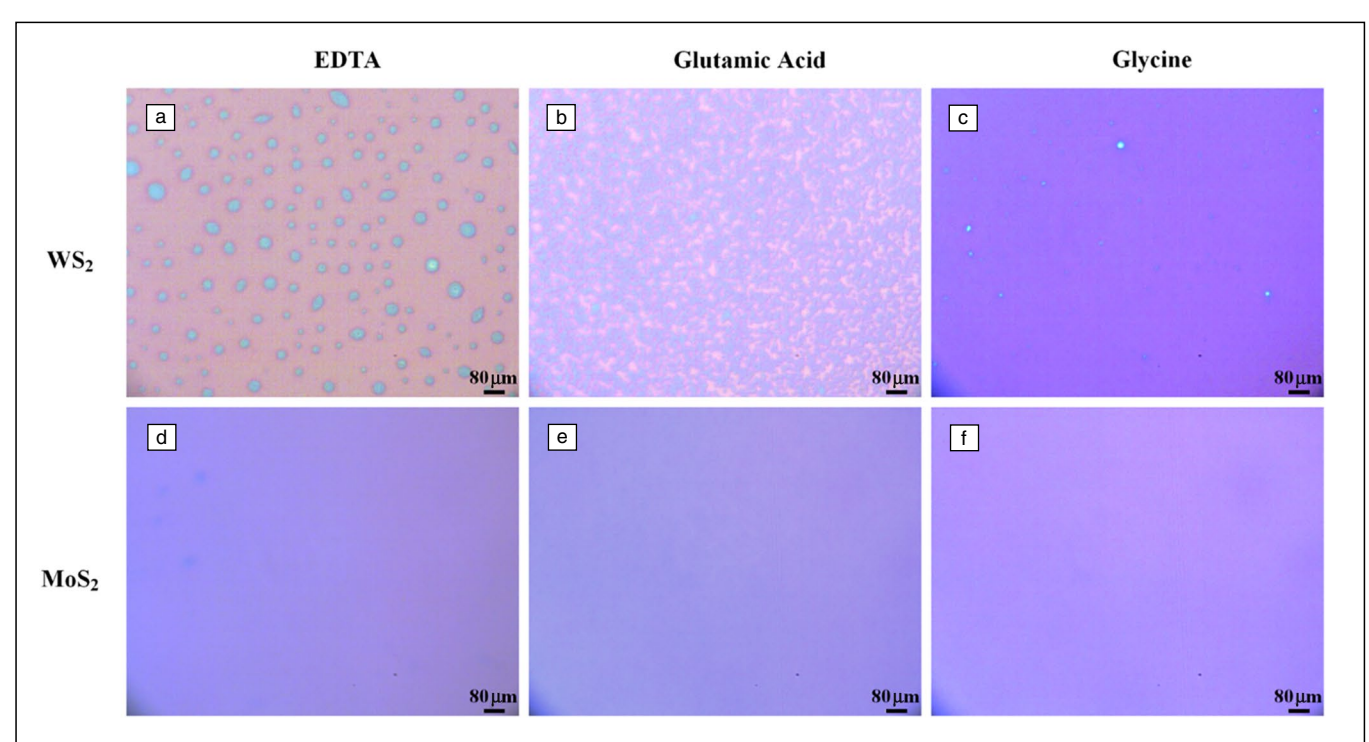


Figure 3. Optical image of transition-metal dichalcogenide thin films: WS₂ thin films (a–c), MoS₂ thin films (d–f). Optical images of the thin films using (a, d) EDTA as the chelant, (b, e) glutamic acid as the chelant, (c, f) glycine as the chelant. The concentration of the precursor and molarity of the chelant are the same for each growth.

each chelant precursor film is discussed further in the following sections.

In this experiment, six samples for each chelant were produced to show consistency. Representative samples of the chelant-assisted growths are shown. In the spin-coat step, each solution produced uniform precursor film with no de-wetted regions, indicating each chelating agent actively assisted wettability. A two-step thermolysis follows the spin-coating with the first step ranging from 250°C to 480°C and the high-temperature hold ranging from 650°C to 900°C. In all cases, no Raman signal was observed if the first hold was below 350°C and the second hold was below 700°C. The pressure within the tube varied from 1 to 500 Torr. The films produced at lower pressures gave stronger signal in PL and Raman spectra due to being in a less oxygen-rich environment. There was no difference in either Raman or PL signal at holds between 750°C and 900°C. Figure 3a-c shows the films synthesized for each WS₂ solution. There are two types of structures seen in these growths other than films: clusters of precursor materials and spotty, nonuniform structures. The ATTT/EDTA chelant solution produced no films, only large clusters (blue structures in panel 3A). In most of these samples, there were clusters of precursor material throughout the substrate that ranged in size from 10 to 80 µm. The ATTT/glutamic acid chelant solution produced a mixture of noncontinuous film and spotty, nonuniform structures. There are no clusters of material present in any of these samples. Although there were some samples with large area growth, the thickness varied throughout the substrate.

The ATTT/glycine chelant solution successfully produced uniform film throughout the substrate for all samples. There were no precursor clusters present, and coverage was uniform as verified by SEM. Figure 4a is a representative sample of WS₂ formed using a solution that did not completely chelate using glutamic acid. There is the presence of a large aggregate and incomplete structures that do not form a film. The large aggregate and the lack of a complete film can be attributed to poor chelation. WS₄²⁻ that has not been passivated can aggregate, whereas unreacted chelating agent can bind to the surface without the metal ion, leaving areas without tungsten precursor. SEM images for Figure 4b-c were taken near an intentionally de-wetted (contrast on the top-left of panel 4b) to be able to focus the instrument. There were no visible structures, so the magnification was increased to 20,000× for panel 4c. What little contrast there is can be attributed to the surface roughness of the underlying SiO₂ substrate. We can deduct from these images that the films (panels 4b-c) are atomically flat with variations of no more than one or two molecule layers. We have corroborated this with Raman mapping, AFM, and STEM imaging in the following sections. Of the three chelants, the glycine-enhanced growths yielded the most consistent results. These results are in contrast with the chelant solutions for MoS₂ Figure 3d-e, which shows the complete films synthesized from (NH₄)₂MoS₄ precursor solutions using the three chelants. Wafer-scale film is produced when using all three chelants with the MoS₄²⁻ precursor.

In all samples of MoS₂, there are no precursor clusters or spotty, nonuniform structures. Although the concentration



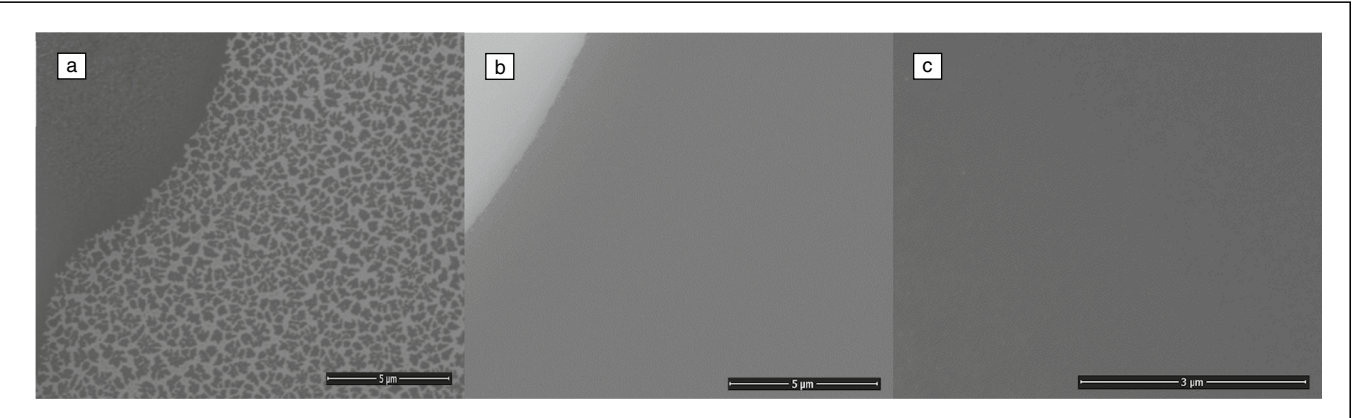


Figure 4. Scanning electron microscope images of WS_2 growths following poor chelation (a) and more complete chelation (b, c). (a) Representative non-film WS_2 structures at $6500 \times$ magnification. The top left (dark gray and textured) and small dark structures are WS_2 , while the light gray is the SiO_2 substrate. (b) The top left (lighter shade of gray) is the exposed SiO_2 surface (de-wetted region), while the rest is continuous WS_2 film (darker gray) at $8000 \times$ magnification. (c) The same WS_2 film in (b) at $20,000 \times$ magnification. Minor contrast is seen here as the film varies by one or two atomic layers throughout.

and spin-coat parameters are the same, there is a slight difference in thickness. The difference between the two salts can be attributed to the ionic clusters it creates in the solution. The tungsten and molybdenum salts used in this study create ionic WS₄²⁻ and MoS₄²⁻ clusters, respectively. As previously discussed, tungsten self-polymerizes into meta-tungstate aggregates if the solution is too acidic. Molybdate polymerization can also occur, but the pH must be more acidic than the pH value required for tungsten complexing.³³ As such, we can derive that the chelating agents used in this study are not acidic enough to produce reactions parasitic to MoS₄²⁻ chelation. If these clusters are insoluble and unstable, they produce de-wetted regions in the film among other types of defects. It has been shown that these salt solutions must be stabilized by the addition of a molecule that can form hydrogen bonds with the cluster's groups.^{23,38} It has been reported that the addition of 2-aminoethanol molecules to the solution can stabilize with the MoS₄²⁻ clusters forming Mo-O-Mo bonds.³⁹ It has been proposed that EDTA form H-bond formation with DMSO and the MoS₄²⁻ cluster.²⁵ In a chelant precursor solution, the chelant is what coordinates and stabilizes the WS₄²⁻ clusters in the solution. For MoS₂, all chelants bind and stabilize MoS₄²⁻, prevent clustering, and promote even anchoring leading to full-film coverage.

Figure 5 shows the Raman and photoluminescence of the TMD monolayers (MoS_2 and WS_2). In Figure 5c, we compared the photoluminescence of the WS_2 monolayer using different chelants. The entire PL spectrum is a combined contribution from neutral exciton X^0 and trion T. We observed minor differences in PL peak positions when using different chelants although the overall PL spectra look similar. ¹⁴ The discrepancy could be attributed to the induced strain by the chelant solution, which leads to a blueshift or redshift of the PL. The comparison of WS_2 Raman with different chelants is shown in Figure 5d. The overall Raman spectra match well with literature ²⁰ and sharp peaks are observed at 355 cm $^{-1}(E_{2g})$

and 418 cm⁻¹(A_{1g}). The FWHM of the A_{1g} and E_{2g} peaks are 7.0 cm⁻¹ and 7.2 cm⁻¹, which are close to that of exfoliated WS₂ monolayers as such the overall Raman spectra indicate good growth quality. We applied a double peak fitting for the neutral exciton (X^0) and the trion (T). The FWHM for the glycine-assisted chelant film were 71 meV and 99 meV, respectively. The larger FWHM could be attributed to the strain induced by the thermolysis of the chelant or a higher defect density than exfoliated WS₂. The nanocrystalline nature of the material and the slight variance could also contribute.

There are three major Raman modes under the excitation of a 532-nm laser, 2LA(M), E^1_{2g} , and A_{1g} , that are used to evaluate the thickness of the material. In this material, the A_{1g} mode blueshifts with increasing layers 35,40 while E^1_{2g} and 2LA(M) redshifts. According to several reports in the literature, the difference in Raman shift, Δv (E^1_{2g} - A_{1g}), is a good indicator of thickness. 41 In **Table** I, the E^1_{2g} , and A_{1g} peak positions can vary. This suggests that other factors are influencing the optical properties that are based on the growth technique used to obtain the material.

In this table, the Δv for monolayers is in the range of 60.5-62.8 cm⁻¹. Although there is a distinction between mono-layers and bilayers, it is difficult to distinguish between a few layered WS₂. In Table I, we see that two to three layered material can have a frequency difference that ranges from 64.5 to 71 cm⁻¹. The PL of WS₂ is a good indicator of crystallinity. In Figure 6, the mechanically exfoliated WS2 is fitted to two Lorentzian functions for the trion and neutral exciton peak. The neutral exciton peak is centered at 2.017 eV, and the full width at half maximum (FWHM) of 29 meV is slightly below the reported value for 1L WS₂ (~47 meV). ^{48,49} The trion peak is centered at 1.97 eV with a FWHM of 78 meV. In comparison, the chelant-enhanced WS2 has a broader full width at half maximum of 50 meV at the same peak center. A broader full width at half maximum and a redshift in PL position are indicative of an increase of defects. 50 The quality of these samples is comparable to CVD film growth in literature.⁵¹



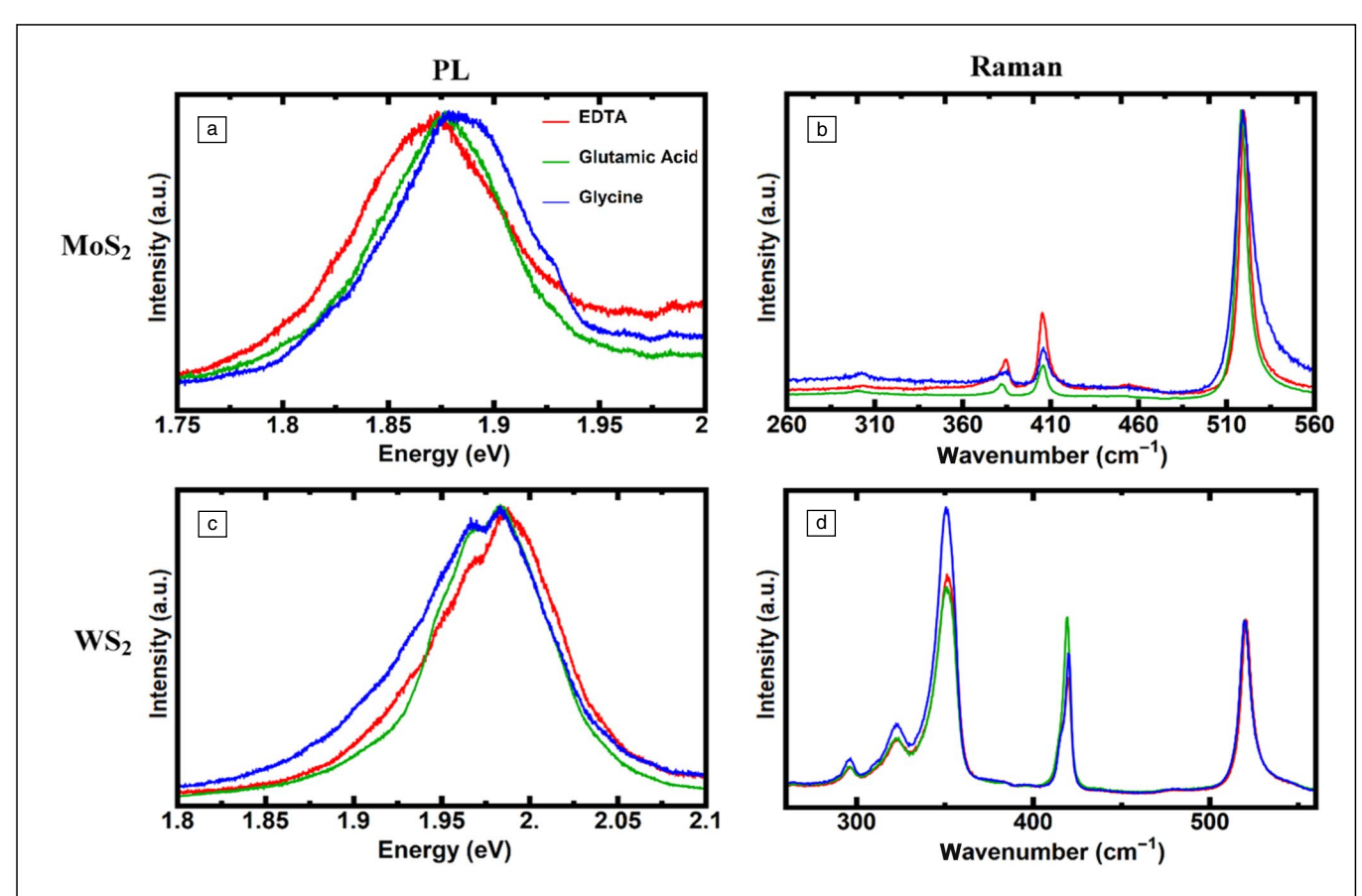


Figure 5. Photoluminescence of transition-metal dichalcogenide (TMD) films (a, c). Raman spectra of TMD films (b, d). MoS₂ thin films (a, b), WS₂ thin films (c, d). The legend shows the three different chelants. EDTA is red, glutamic acid is green, and glycine is blue. The photoluminescence spectra are normalized to show the difference in energy position (eV). The Raman spectra are normalized by setting the silicon peak as the reference point.

Table I. A comparison of Raman peak positions for different types of growth methods using a 532-nm laser excitation.							
Growth Method	Material	Layers	E ¹ _{2g} (cm ⁻¹)	A _{1g} (cm ⁻¹)	$\textbf{A}_{1\textbf{g}}-\textbf{E}_{2\textbf{g}}^{1}$	$\textbf{A}_{1\textbf{g}}/\textbf{E}_{2\textbf{g}}^{1}$	Domain
APCVD of WO ₃ precursor on SiO ₂ ⁴⁰	Triangle	1	352.5	419	66.5	0.21	~400 µm
		2			71	0.5	
APCVD of powder WO ₃ on SiO ₂ ⁴²	Triangle	1	355	417	62		
		2	354	418.5	64.5		
Sulfurization of W thin film on sapphire by sputtering method ⁴³	Large area films	1	357.2	420	62.8		
		2	355.1	421.1	66		
Mechanically exfoliated ⁴⁴	Flake	1	352.1	417.5	65.4		
		2	350.9	418.3	67.4		
		3	349.8	418.7	68.9		
Mechanically exfoliated (this work)	Flake	1	356.5	417	60.5	0.203	
Thermal decomposition of chelated $(\mathrm{NH_4})_2\mathrm{WS_4}$ in solution (this work)	Large area films	1	356.4	418	61.6	0.28	
LPCVD of W(CO) ₆ precursor on SiO ₂ ⁴⁵	Large area films	1	355.2	417.2	62		5–10 nm
Sulfurization of W thin films on MgO deposited by magnetron sputtering method ⁴⁶	Large area films	1	352.7	414.7	62		50–200 nm
Sulfurization of WO_3 thin film prepared by atomic layer deposition 47	Large area films	5	354.7	419.7	65	0.78	
LPCVD of WO ₃ precursor on sapphire ⁴³	Triangle	1	354.4	416.8	62.4		~50 µm

The A_{1g} , and E_{2g} peak positions of WS $_2$ synthesized by the various methods found in literature highlighted here. The difference between A_{1g} and E_{2g} (Δv) can vary by 2–2.5 cm $^{-1}$.



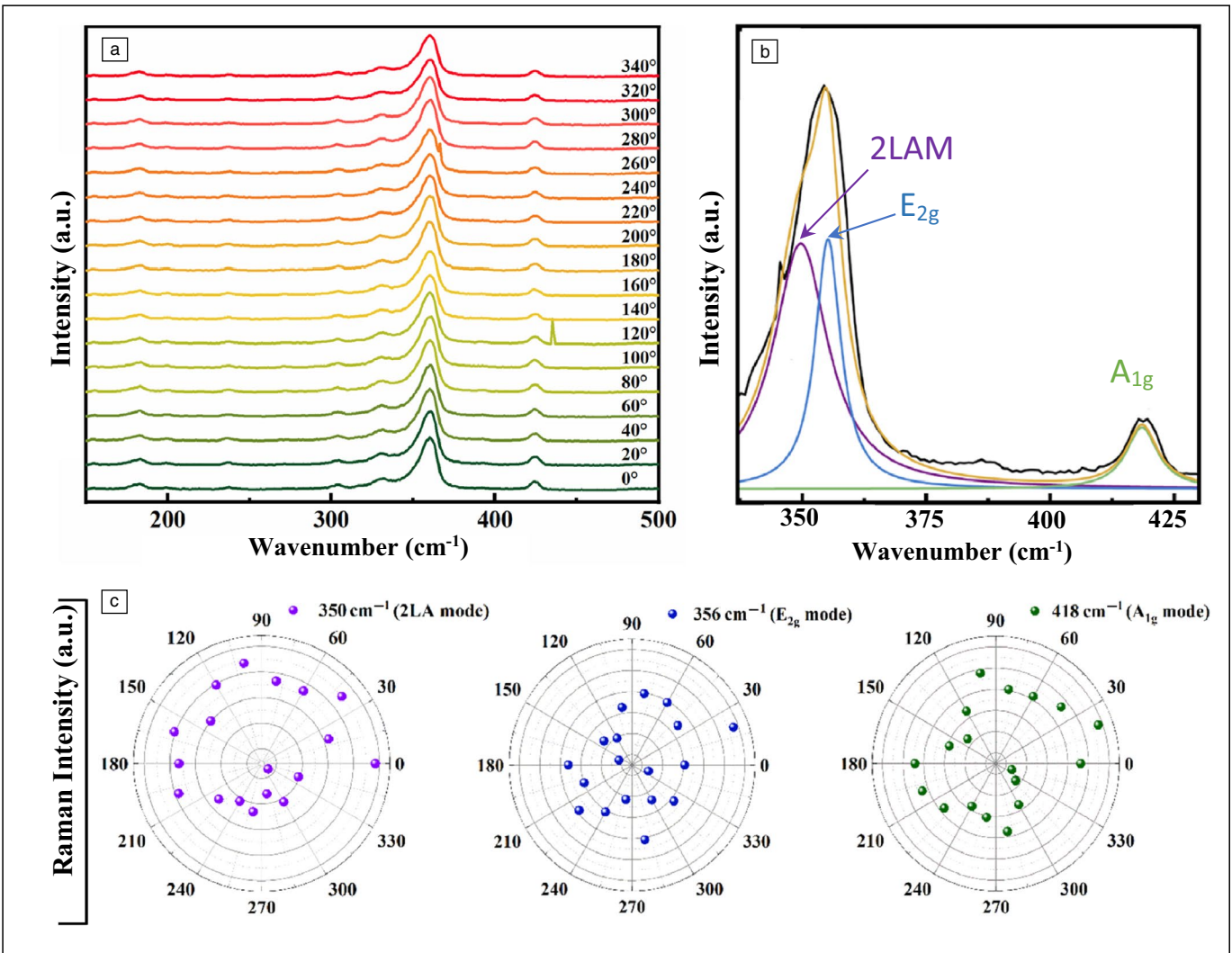


Figure 6. Angle-resolved Raman spectroscopy of WS $_2$. (a) Raman spectrum over various angles. (b) Fitting parameters for the 2LA, E_{2g} , and A_{1g} peaks for the Raman spectrum. (c) Polar plots of the Raman intensities 2LA, E_{2g} , and A_{1g} .

Figure 6c shows angle-resolved spectroscopy of glycine-enhanced WS₂ film. We focus on the 2LA (350 cm⁻¹), E_{2g} (356 cm⁻¹), and A_{1g} (418 cm⁻¹) modes and perform a polar plot to show the angle-dependent intensity of these modes. Previous reports on other transitional-metal dichalcogenide materials suggest isotropic behavior when the polarization is in *ab* plane.⁵² The intensity variation with respect to angles in our study could also induced by the integrated contribution of different grains. To be more specific, the lattice direction can vary in different grains so that the Raman intensity which is dependent on the Raman tensor is not perfectly isotropic. We also observed an intensity drop, which is due to laser damage to the monolayer.

The overall uniformity and quality of the synthesized WS₂ film was explored via Raman mapping in **Figure** 7. An area the size of 50 μ m² was scanned in 0.80 μ m steps with an excitation wavelength of 532 nm. From the spectra, we extracted the peak positions of the A_{1g} and E_{2g} modes whose frequency difference and intensity ratios are indicators of layer

thickness and quality. 41,47 All spectra were normalized relative to silicon's intensity at 520 cm⁻¹. From Figure 7a, we see the majority of the spectra overlap, which indicates consistency. In Figure 7b–c, the frequency differences and intensity ratios are plotted against the 50 × 50-μm Raman map to see how sample thickness varies spatially. We see in Figure 4b that the frequency difference sits largely around 67 cm⁻¹, which would indicate the area is bi- to few layer. Table I shows that while the frequency difference varies (with anything above 65 cm⁻¹ potentially indicating five layers), the peak intensity ratio seems consistent. A ratio of A_{1g}/E_{2g} of 0.78 is indicative of five layered WS2, whereas a ratio of 0.2 denotes films at the monolayer limit. Figures 4c and 9(d-f) show that the film is largely few layer and bilayer. The map also shows that the ratio is well below five layers of WS2 as the threshold ratio is 0.78.47

To confirm the implied layer thickness from the Raman mapping, we have performed AFM. The produced glycine/ATTT films are uniform and completely cover the substrate.

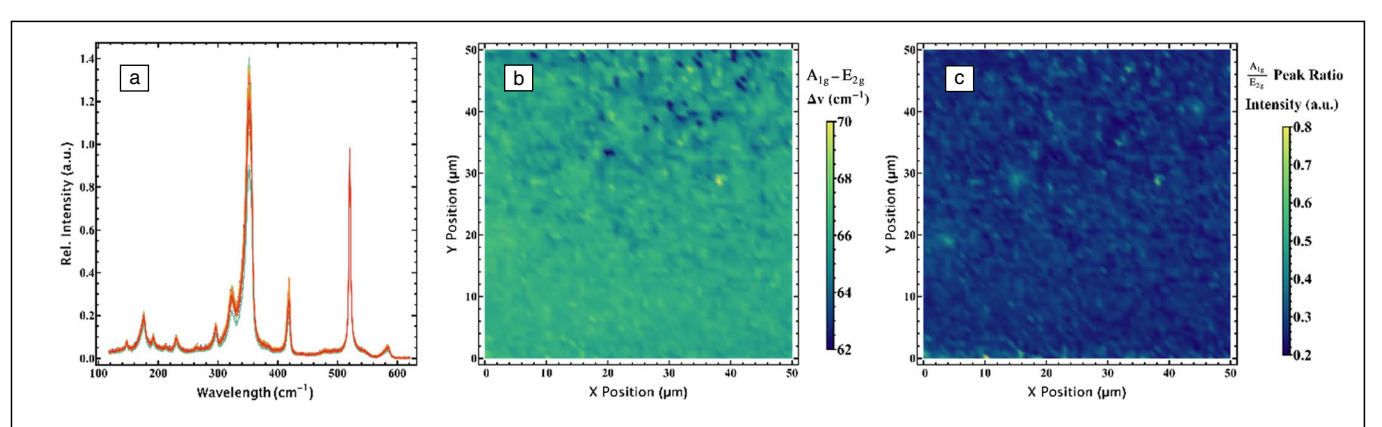


Figure 7. (a) The combined Raman spectra of a 50×50 -µm map plotted together to examine homogeneity. All spectra were normalized to silicon's relative intensity at 520 cm^{-1} . (b) A 2D map of the A_{1g} and E_{2g} difference over a 50×50 -µm area was performed to examine overall layer uniformity. (c) The ratio of peak intensity of the A_{1g}/E_{2g} modes.

As there is no exposed SiO₂ in un-cleaved samples, a sample with de-wetted regions was prepared. The substrate was repeatedly scratched with a diamond scribe to introduce pieces of bare silicon, which are hydrophobic and would yield regions without film. AFM was done near an intentionally dewetted region to show what the material thickness is, as can be seen in **Figure** 8a. Figure 8b depicts a height profile of the de-wetted region. Due to the low surface energy caused by the de-wetting, the material is removed and accumulated at the edge of the material. The thickness of the film approximately varies between 2.6 and 3.5-nm thick with a surface roughness of 0.683 nm and is consistent with few layers of WS₂. ³⁰ This film's thickness corresponds to three to four atomic layers of WS₂, which is consistent with the Raman mapping.

A representative sample of the ATTT-glycine derived WS₂ was transferred onto a quantifoil TEM grid for ADF-STEM imaging to analyze the atomic structure of the film. Figure 9a–c shows low to intermediate magnification ADF-STEM imaging of the basal plane {0001} of the film. In these

а

4 μm

lower magnification images (Figure 9a-c), the amorphous carbon backing is reducing the contrast making it difficult to see the potential difference in layers. In Figure 9a, we see a continuous film (>20 µm) with little contrast showing the chelating agent helped disperse the WS₄²⁻ precursor more evenly. Figure 9b-c are higher magnification and also show little contrast showcasing the general flatness of the films. Figure 9d shows an HAADF-STEM stacking of the WS2 layers and the inset shows the Z-contrast of the tungsten and sulfur atoms. The synthesized films are multilayered, and their stacking can clearly be seen in Figure 9e-f. Fast Fourier transform was performed on images Figure 9d-f to see what WS₂ polymorph we synthesized and to understand the stacking of the layers. The fully indexed fast Fourier transform of Figure 9d (Figure 9g) is consistent with the 2H (hexagonal) polymorph of WS₂.⁵¹ Figure 9h-i are the FFT of Figure 9e-f, respectively, in which the nanodomain is imaged down its [0001] axis. The estimated twist angle was measured between the 000 beam and two successive diffraction spots. In both cases,

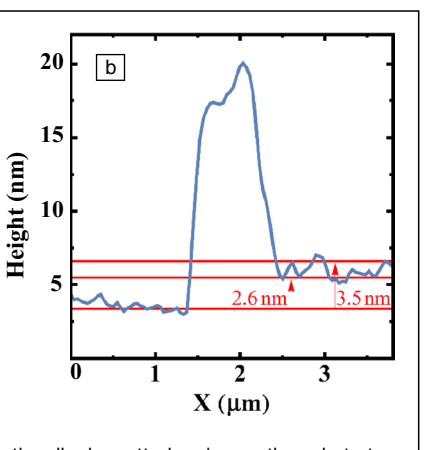


Figure 8. (a) Atomic force microscopy of WS_2 film at an intentionally de-wetted region on the substrate. After spin coating, the film forms. The solution does not relax on the surface due to hydrophobicity of the area near the de-wetted region. The solution concentrates itself near the edges of the de-wetted region forming a thick layer of material. (b) A line scan done across step in thickness. The thickness of the film ranges from 2.6 to 3.5 nm.

27.0 nm

20.0

15.0

10.0

5.0

0.0

six measurements were taken, and the average and standard deviation was determined. The twist angles derived from the FFT in Figure 9h ranged from 23.1 to 25.3° with an average of $23.98^{\circ} \pm 1.02$. For the FFT in Figure 9i, the twist angles ranged from 25.3 to 26.9° with the average being $26.38^{\circ} \pm 0.65$. From these random stacked angles, we can see that the atomic arrangement of tungsten and sulfur differ from structures with 0° angles. Our HAADF-STEM results closely match with the distorted moiré lattice patterns found in WS₂ with similar rotation angles.⁵³



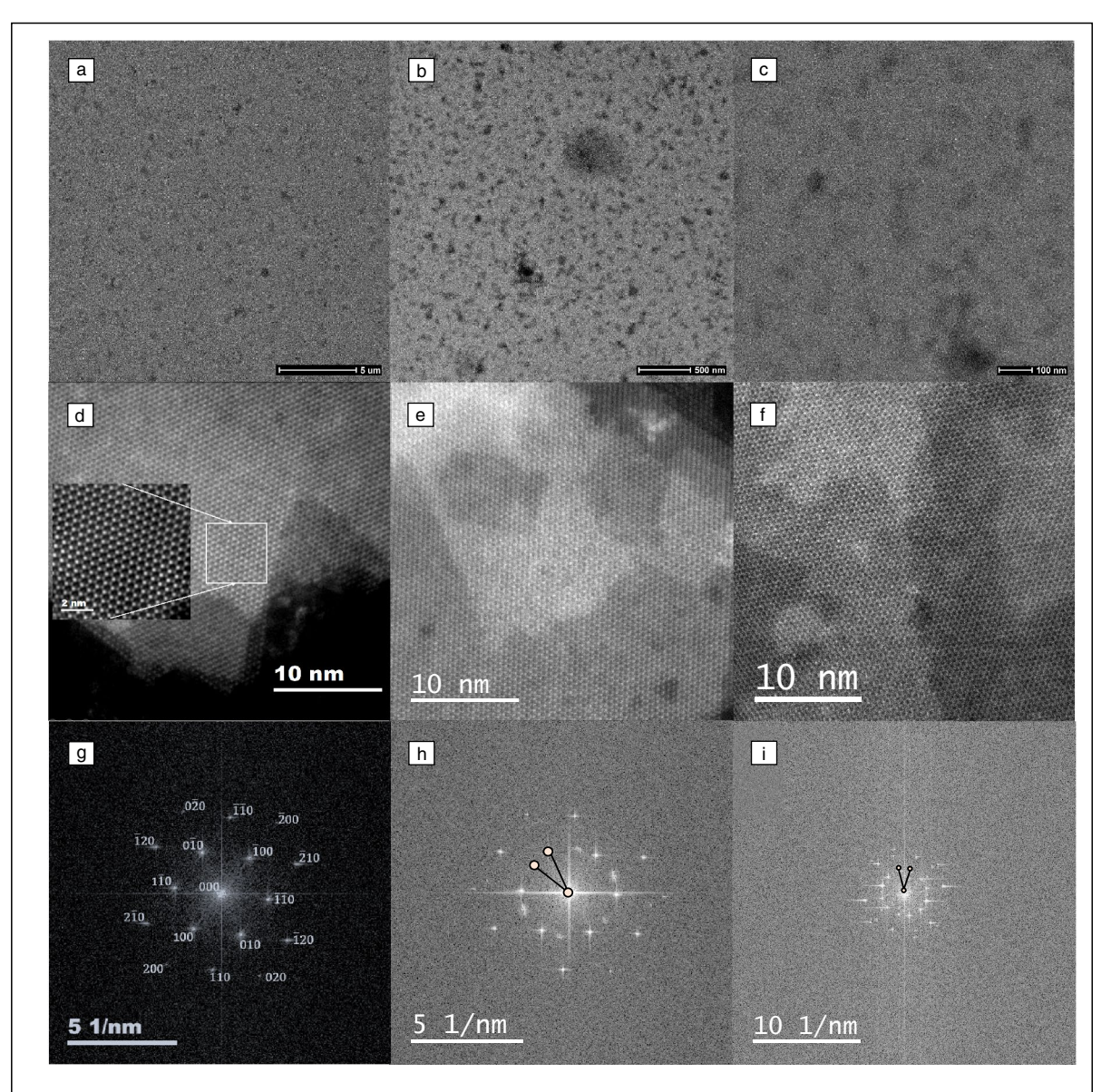


Figure 9. Transmission electron microscope images of the synthesized WS_2 . (a) Low magnification image showing the transferred continuous WS_2 film. (b) A higher magnification image of a region found in (a). (c) An intermediate magnification image with low contrast showing the variation in thickness. (d) High-angle annular dark-field scanning transmission electron micrograph (STEM) of the synthesized WS_2 . Thin-film inset: high-resolution STEM showing Z-contrast between the tungsten and sulfur atoms. (e, f) Stacking and multiple layers of the as-synthesized WS_2 film. (g) Fully indexed fast Fourier transform (FFT) of (d) that matches consistently with the established literature. (h, i) FFT of panels (e, f), respectively. (h, i) Two diffraction spots and how the twist angle was estimated between the 000 beam.

In conclusion, we have presented results on the growth of WS₂ using ATTT and three different chelating agents in DMSO. This work has found that molecules containing carboxylate and amino groups can favorably bind to SiO₂, thereby enhancing film coverage and uniformity by improved wettability. Whereas the chelant used had little effect on MoS₂ growth, only glycine was shown to produce uniform films of WS₂. Completeness in film coverage improves as we go from EDTA, to glutamic acid, to glycine. Two trends can be reasonably attributed to the progressive increase in film coverage: the relative size of the molecule, and the acidity of the molecule. As film coverage increases,

both the relative size of the molecule and acidity decline, implying that both or one of these factors into the final film coverage. By incorporating various chelants containing these carboxylate and amino groups, we have enabled the solution-based growth of WS₂ at the wafer scale. UV vis confirmed the chelation of WS₄²⁻ with glycine while Raman and AFM confirmed the growth of few-layer WS₂ films. This work provides the basis for further study of chelating agents amenable to solution-based processing of thin-film materials on oxides. Film thickness and uniformity could be improved by designing a chelating agent with a more compatible size and relative acidity.



Methods

Dichalcogenide layer synthesis

The thin films were synthesized onto 300-nm $\mathrm{SiO_2/Si}$ substrates by the thermolysis of spin-coated films. The substrates were cleaned by sonification in acetone and then in isopropanol for 30 min each. The substrates are then submersed in RCA SC-1 solution (five parts DI water, one part NH₄OH, one part H₂O₂) at 80°C for 10 min. This is followed by a DI water rinse. To enhance the wettability of our substrates, an RCA Clean was performed followed by O₂ plasma treatment for 10 min. This cleans the substrate and introduces surface hydroxyl groups.

Three solutions with 0.1 M of each chelant were prepared in dimethyl sulfoxide (DMSO); 45 mg of ammonium tetrathiotungstate (Sigma Aldrich high purity 99.99%) were added and dissolved. The solution was stirred for 3 h. The solution is then filtered using a 1-µm polycarbonate filter followed by a 0.2-µm polycarbonate filter. The solution is stored for 24 h before use. The solution is then sonicated for 30 min, then immediately applied to the substrate. The substrate is spin-coated at 3000 rpm for 60 s. After the spin coat, the sample is immediately placed in the furnace. The substrate is annealed at 100°C in a vacuum (1 Torr) for 30 min.

The substrate is then annealed in a two-step process. The sample is placed in a vacuum in 100 sccm Ar/50 sccm $\rm H_2$ gas flow. The substrate is then annealed at 480°C for 60 min to complete the thermolysis of the film. To improve the crystallinity of the film, the substrate is heated to 800°C for 10 min under a gas flow of Ar (200 sccm). Sulfur is introduced by heating a sulfur boat to 200°C. The system is then slowly cooled to room temperature. The sample is then removed for characterization. Raman and PL spectroscopy were done with a Horiba LabRam HR spectrometer with an excitation wavelength of 532 nm and a laser power of 30 mW with a $100 \times$ objective.

Layer transfer

To obtain TEM imaging, the samples were cleaved from the first spin-coating PMMA at 3000 rpm for 1 min, then allowed to cure overnight at room temperature. The sample was then immersed in a 15 M KOH until the caustic solution released the WS₂/PMMA film. The film was then fished out with a TEM grid, thoroughly rinsed in de-ionized water, and placed in acetone to remove the PMMA. The grid was thoroughly rinsed with de-ionized water after the removal of the PMMA.

Optical spectroscopy

PL and Raman spectra were measured using a 532-nm laser excitation in a backscattering configuration with 1200/mm grating. The laser spot size was $\sim\!\!2~\mu m$. The laser power at the sample is 1.3 mW for Raman and 750 μW for PL measurements. Angle-resolved Raman is performed in our homemade

Raman spectroscopy. The power is 750 μ W to avoid damage to the TMD monolayer. A quarter-wave plate was placed in the incident light path to produce a circularly polarized laser and a polarizer is used to change the polarization.

TEM imaging

High-angle annular dark-field (HAADF) scanning transmission electron micrograph (STEM) of the synthesized WS $_2$ film was performed in NION ultraSTEM 100 at 60-keV acceleration voltage and 30-mrad convergence semi-angle. The samples were baked at 120°C UHV for 8 h prior to measurement to avoid any contamination of the electron-beam column.

SEM

The surface morphology and elemental distribution of the samples were obtained by scanning electron microscopy (SEM, NovaNanoSEM 450) equipped with energy-dispersive x-ray spectroscopy (EDS). The substrate was mounted on carbon tapes before being transferred to the SEM chamber. The pressure of the chamber was as low as 5×10^{-10} Torr under room temperature during the electrical characterization. All SEM and EDX characterization were performed under accelerating voltage of 20 kV and emission current of 70 μ A.

DFT computations

The simulations were performed by the Quantum ESPRESSO package. 54,55 Generalized gradient approximations in the form of Perdew-Burke-Ernzerhof (PBE) were utilized for the exchange-correlation interactions.⁵⁶ The ion-electron interactions were characterized by ultrasoft pseudopotentials.⁵⁷ A smearing function was also used for an electronic system. 40 A kinetic energy cutoff of 50 Ry was employed for the wave function and a charge density cutoff of 600 wave functions and a charge density cutoff of 600 Ry were used. The Broyden-Fletcher-Goldfarb-Shanno (BFGS) algorithm has been implemented to optimize the studied structures. The maximum force and energy on each atom were 0.001 eV Å and 10-6 eV/atom, respectively. To minimize periodic interactions, we chose a vacuum space greater than 15 Å along the z-direction of the SiO₂ surface. Moreover, many initial binding points were tested to get the possible structure with the lowest total energy between chelating agents and SiO₂ interactions. The binding energies E_h are then calculated by the equation,

$$E_b = (E_{\text{molecule}} + E_{\text{SiO}_2}) - E_{\text{molecule} + \text{SiO}_2},$$

where $E_{\rm molecule}$ is the total energy of the chelating agent, $E_{\rm SiO2}$ is the total energy of the SiO₂, and $E_{\rm molecule+SiO2}$ is the total energy of chelating agents – SiO₂ system. To understand the interactions between the three chelants glycine, glutamic acid, and EDTA and metal ions of (NH₄)₂WS₄ in DMSO, the Gaussian 09 program package was used based on the B3LYP functional with CEP-121G basis set in DMSO^{58–60} and VESTA was used for visualization. 61



Acknowledgments

Financial support for this work was provided by the STARnet center, C-SPIN (Center for Spintronic Materials, Interfaces, and Novel Architectures, Grant No. MARCO-A003571404), through the SRC (Semiconductor Research Corporation) sponsored by the MARCO (Microelectronics Advanced Research Corporation) and DARPA (Defense Advanced Research Projects Agency); the DOE (Department of Energy) Grant. No. DOE-SC0020653; the NSF (National Science Foundation) Grant No. CMMI (Civil, Mechanical and Manufacturing Innovation) -1825594, CMMI-1933214, DMR (Division of Materials Research) -1955889, DMR-1904716, DMR-2111812, and ECCS (Electrical, Communications and Cyber Systems) -2052527. Finally, DFT (density functional theory) and energy minimization computations were performed at the TÜBITAK ULAKBİM High Performance and Grid Computing Center (TRUBA Resources) in Ankara, Turkey.

Funding

Funding was provided by Microelectronics Advanced Research Corporation (Grant No. A003571404) [National Science Foundation (Grant No. 1955889), TÜBITAK ULAKBİM Supercomputer Center—National Science Foundation (Turkey) and National Science Foundation (Grant No. 2052527)].

Data availability

All data generated or analyzed during this study are included in this published article.

Conflict of interest

The authors have no competing interests to declare that are relevant to the content of this article.

References

- 1. Y. Shi, H. Li, L.J. Li, *Chem. Soc. Rev.* 44, 2744 (2015)
- 2. S. Das, H.-Y. Chen, A.V. Penumatcha, J. Appenzeller, *Nano Lett.* **13**(1), 100 (2013)
- 3. B. Radisavljevic, M.B. Whitwick, A. Kis, ACS Nano 5, 9934 (2011)
- X. Liu, J. Hu, C. Yue, N. Della Fera, Y. Ling, Z. Mao, J. Wei, ACS Nano 8, 10396 (2014)
 J.S. Ross, S. Wu, H. Yu, N.J. Ghimire, A.M. Jones, G. Aivazian, J. Yan, D.G. Mandrus,
 D. Xiao, W. Yao, X. Xu, Nat. Commun. 4, 1474 (2013)
- K.F. Mak, C. Lee, J. Hone, J. Shan, T.F. Heinz, *Phys. Rev. Lett.* **105**, 136805 (2010)
 T. Cao, G. Wang, W. Han, H. Ye, C. Zhu, J. Shi, Q. Niu, P. Tan, E. Wang, B. Liu, J. Feng, *Nat. Commun.* **3**, 887 (2012)
- 8. A. Castellanos-Gomez, M. Barkelid, A.M. Goossens, V.E. Calado, H.S.J. Van Der Zant, G.A. Steele, *Nano Lett.* **12**, 3187 (2012)
- 9. G. Eda, H. Yamaguchi, D. Voiry, T. Fujita, M. Chen, M. Chhowalla, *Nano Lett.* 11, 5111 (2011)
- 10. B. Radisavljevic, A. Radenovic, J. Brivio, V. Giacometti, A. Kis, *Nat. Nanotechnol.* **6**, 147 (2011)
- 11. H. Li, J. Wu, Z. Yin, H. Zhang, Acc. Chem. Res. 47, 1067 (2014)
- 12. A. Splendiani, L. Sun, Y. Zhang, T. Li, J. Kim, C.-Y. Chim, G. Galli, F. Wang, *Nano Lett.* **10**, 1271 (2010)
- 13. S. Berciaud, S. Ryu, L.E. Brus, T.F. Heinz, *Nano Lett.* **9**, 346 (2009)
- 14. Y. Chen, J. Xi, D.O. Dumcenco, Z. Liu, K. Suenaga, D. Wang, Z. Shuai, Y.S. Huang, L. Xie, *ACS Nano* **7**, 4610 (2013)
- 15. A.M. Van Der Zande, P.Y. Huang, D.A. Chenet, T.C. Berkelbach, Y. You, G.H. Lee,
- T.F. Heinz, D.R. Reichman, D.A. Muller, J.C. Hone, *Nat. Mater.* **12**, 554 (2013) 16. Y. Lee, X. Zhang, W. Zhang, M. Chang, C. Lin, K. Chang, Y. Yu, J.T. Wang, C. Chang, L. Li, T. Lin, *J. Mater. Chem.* **10**, 2320 (2012)
- 17. B. Liu, M. Fathi, L. Chen, A. Abbas, Y. Ma, C. Zhou, ACS Nano 9, 6119 (2015)
- 18. Y. Zhan, Z. Liu, S. Najmaei, P.M. Ajayan, J. Lou, Small 8, 966 (2012)
- 19. C.M. Orofeo, S. Suzuki, Y. Sekine, H. Hibino, Appl. Phys. Lett. 105, 83112 (2014)

- J.G. Song, J. Park, W. Lee, T. Choi, H. Jung, C.W. Lee, S.H. Hwang, J.M. Myoung, J.H. Jung, S.H. Kim, C. Lansalot-Matras, H. Kim, ACS Nano 7, 11333 (2013)
- 21. K.K. Liu, W. Zhang, Y.H. Lee, Y.C. Lin, M.T. Chang, C.Y. Su, C.S. Chang, H. Li, Y. Shi, H. Zhang, C.S. Lai, L.J. Li, *Nano Lett.* **12**, 1538 (2012)
- 22. A.S. George, Z. Mutlu, R. Ionescu, R.J. Wu, J.S. Jeong, H.H. Bay, Y. Chai, K.A. Mkhoyan, M. Ozkan, C.S. Ozkan, *Adv. Funct. Mater.* **24**, 7461 (2014)
- 23. J. Yang, Y. Gu, E. Lee, H. Lee, S.H. Park, M.H. Cho, Y.H. Kim, Y.H. Kim, H. Kim, *Nanoscale* **7**, 9311 (2015)
- 24. Y.R. Lim, W. Song, J.K. Han, Y.B. Lee, S.J. Kim, S. Myung, S.S. Lee, K.S. An, C.J. Choi, J. Lim, *Adv. Mater.* **28**, 5025 (2016)
- 25. R. Ionescu, B. Campbell, R. Wu, E. Aytan, A. Patalano, I. Ruiz, S.W. Howell, A.E. McDonald, T.E. Beechem, K.A. Mkhoyan, M. Ozkan, C.S. Ozkan, *Sci. Rep.* 7(1), 6419 (2017)
- 26. Y.H. Hung, A.Y. Lu, Y.H. Chang, J.K. Huang, J.K. Chang, L.J. Li, C.Y. Su, ACS Appl. Mater. Interfaces 8, 20993 (2016)
- H. Yang, A. Giri, S. Moon, S. Shin, J.M. Myoung, U. Jeong, *Chem. Mater.* 29, 5772 (2017)
- 28. Z. Li, S. Jiang, S. Xu, C. Zhang, H. Qiu, P. Chen, S. Gao, B. Man, C. Yang, M. Liu, *J. Alloys Compd.* **666**, 412 (2016)
- 29. K.C. Kwon, C. Kim, Q. Van Le, S. Gim, J.M. Jeon, J.Y. Ham, J.L. Lee, H.W. Jang, S.Y. Kim, *ACS Nano* 9, 4146 (2015)
- 30. O.A. Abbas, I. Zeimpekis, H. Wang, A.H. Lewis, N.P. Sessions, M. Ebert, N. Aspiotis, C.C. Huang, D. Hewak, S. Mailis, P. Sazio, *Sci. Rep.* **10**, 1696 (2020)
- 31. J.W. McDonald, G.D. Friesen, L.D. Rosenhein, W.E. Newton, *Inorganica Chim. Acta* 72, 205 (1983)
- 32. S. Badoga, K.C. Mouli, K.K. Soni, A.K. Dalai, J. Adjaye, *Appl. Catal. B* **125**, 67 (2012) 33. R.J. Kula, D.L. Rabenstein, *Anal. Chem.* **38**, 1934 (1966)
- 34. P.K. Panigrahi, A. Pathak, *Sci. Technol. Adv. Mater.* **9**(4), 045008 (2008). https://doi.org/10.1088/1468-6996/9/4/045008
- 35. P. Liu, T. Luo, J. Xing, H. Xu, H. Hao, H. Liu, J. Dong, *Nanoscale Res. Lett.* 12, 558 (2017)
- 36. S. Yamabe, N. Ono, N. Tsuchida, J. Phys. Chem. A 107, 7915 (2003)
- 37. A.A. Agzamkhodzhaev, L.T. Zhuravlev, A.V. Kiselev, K.Y. Shengeliya, *Bull. Acad. Sci. USSR Div. Chem. Sci.* **18**, 1968 (1969)
- 38. J. Pütz, M.A. Aegerter, J. Solgel Sci. Technol. 26, 807 (2003)
- 39. A. Müller, E. Diemann, R. Jostes, H. Bögge, *Angew. Chem Int. Ed.* **20**(11), 934 (1981)
- 40. A. Berkdemir, H.R. Gutiérrez, A.R. Botello-Méndez, N. Perea-López, A.L. Elías, C-.l. Chia, B. Wang, V.H. Crespi, F. López-Urías, J.-C. Charlier, H. Terrones, M. Terrones, *Sci. Rep.* **3**(1), 1755 (2013)
- 41. N. Peimyoo, J. Shang, W. Yang, Y. Wang, C. Cong, T. Yu, Nano Res. 8, 1210 (2015)
- 42. A. Thangaraja, S.M. Shinde, G. Kalita, M. Tanemura, *Mater. Lett.* **156**, 156 (2015) 43. Y. Zhang, Y. Zhang, Q. Ji, J. Ju, H. Yuan, J. Shi, T. Gao, D. Ma, M. Liu, Y. Chen, X. Song, H.Y. Hwang, Y. Cui, Z. Liu, *ACS Nano* **7**, 8963 (2013)
- 44. S. Qiao, H. Yang, Z. Bai, G. Peng, X. Zhang, Energy Environ. 141, 1408 (2017)
- 45. S. Cadot, O. Renault, D. Rouchon, D. Mariolle, E. Nolot, C. Thieuleux, L. Veyre, H. Okuno, F. Martin, E.A. Quadrelli, *J. Vac. Sci. Technol. A* **35**, 061502 (2017)
- 46. C.M. Orofeo, S. Suzuki, Y. Sekine, H. Hibino, *Appl. Phys. Lett.* **105**(8), 083112 (2014). https://doi.org/10.1063/1.4893978
- 47. M.G. Kozodaev, A.S. Slavich, R.I. Romanov, S.S. Zarubin, A.M. Markeev, *J. Phys. Chem. C* 124, 28169 (2020)
- 48. W. Zhao, Z. Ghorannevis, L. Chu, M. Toh, C. Kloc, P.-H. Tan, G. Eda, *ACS Nano* **7**(1), 791 (2013)
- 49. W. Shi, M.-L. Lin, Q.-H. Tan, X.-F. Qiao, J. Zhang, P.-H. Tan, *2D Mater.* **3**(2), 025016 (2016). https://doi.org/10.1088/2053-1583/3/2/025016
- J. Li, W. Su, F. Chen, L. Fu, S. Ding, K. Song, X. Huang, L. Zhang, J. Phys. Chem. C 123, 3900 (2019)
- 51. A. McCreary, A. Berkdemir, J. Wang, M.A. Nguyen, A.L. Elías, N. Perea-López, K. Fujisawa, B. Kabius, V. Carozo, D.A. Cullen, T.E. Mallouk, J. Zhu, M. Terrones, *J. Mater. Res.* **31**(7), 931 (2016)
- 52. M. Jin, W. Zheng, Y. Ding, Y. Zhu, W. Wang, F. Huang, *J. Phys. Chem. C* 10, 2 (2019) 53. G. Shao, X.X. Xue, X. Liu, D. Zhang, Y. Jin, Y. Wu, B. You, Y.C. Lin, S. Li, K. Suenaga, X. Wang, A. Pan, H. Li, J. Hong, Y. Feng, S. Liu, *Chem. Mater.* 32, 9721 (2020)
- 54. S. Scandolo, P.I. Giannozzi, C.I. Cavazzoni, S.I. de Gironcoli, A.V. Pasquarello, S.I. Baroni, *J. Mater. Chem.* **220**, 574 (2005)
- 55. P. Giannozzi, S. Baroni, N. Bonini, M. Calandra, R. Car, C. Cavazzoni, D. Ceresoli, G.L. Chiarotti, M. Cococcioni, I. Dabo, A. Dal Corso, S. de Gironcoli, S. Fabris, G. Fratesi, R. Gebauer, U. Gerstmann, C. Gougoussis, A. Kokalj, M. Lazzeri, L. Martin-Samos, N. Marzari, F. Mauri, R. Mazzarello, S. Paolini, A. Pasquarello, L. Paulatto, C. Sbraccia, S. Scandolo, G. Sclauzero, A.P. Seitsonen, A. Smogunov, P. Umari, R.M. Wentzcovitch, *J. Phys. Condens. Matter* 21(39), 395502 (2009). https://doi.org/10.1088/0953-8984/21/39/395502
- 56. J.P. Perdew, K. Burke, M. Ernzerhof, *Phys. Rev. Lett.* **77**, 3865 (1996)
- 57. G. Makov, M.C. Payne, Phys. Rev. B 51, 4014 (1995)
- 58. M.J. Fadhul, G.W. Trucks, H.B. Schlegel, G.E. Scuseria, M.A. Robb, J.R. Cheeseman, G. Scalmani, V. Barone, B. Mennucci, G.A. Petersson, *J. Nonlinear Opt. Phys. Mater.* 27, 1850 (2018)

CHELANT-ENHANCED SOLUTION FOR WAFER-SCALE SYNTHESIS OF FEW-LAYER WS_2 FILMS



59. R.G.P.C. Lee, W. Yang, *Phys. Rev.* **10**, 785 (1988) 60. P.G.J.W.J. Stevens, M. Krauss, H. Basch, *Can. J. Chem.* **10**, 612 (1992) 61. K. Momma, F. Izumi, J. Appl. Crystallogr. 44, 1272 (2011)

Publisher's note Springer Nature remains neutral with regard to jurisdictional claims in published maps and institutional affiliations.

Springer Nature or its licensor (e.g. a society or other partner) holds exclusive rights to this article under a publishing agreement with the author(s) or other rightsholder(s); author self-archiving of the accepted manuscript version of this article is solely governed by the terms of such publishing agreement and applicable law.